JGR Atmospheres

RESEARCH ARTICLE
10.1029/2023JD040227

Using Satellite Observations of Lightning and Precipitation to Diagnose the Behavior of Deep Convection in Tropical Cyclones Traversing the Midlatitudes

Lena Heuscher[1,2], **Patrick Gatlin**[3], **and Walter A. Petersen**[3]

[1]Department of Atmospheric and Earth Science, University of Alabama in Huntsville, Huntsville, AL, USA, [2]Cooperative Institute for Meteorological Satellite Studies/Space Science Engineering Center, University of Wisconsin-Madison, Madison, WI, USA, [3]NASA Marshall Space Flight Center, Huntsville, AL, USA

Key Points:

- This study provides the first characterization of lightning in tropical cyclones (TCs) that have undergone extratropical transition
- Lightning activity within TCs exhibits a unimodal radial distribution as well as for tropical storm and extratropical phases
- TC phase convective differences are driven by both the frequency of lightning producing cells and intensity differences among them

Correspondence to:
L. Heuscher,
heuscherstew@wisc.edu

Citation:
Heuscher, L., Gatlin, P., & Petersen, W. A. (2024). Using satellite observations of lightning and precipitation to diagnose the behavior of deep convection in tropical cyclones traversing the midlatitudes. *Journal of Geophysical Research: Atmospheres*, *129*, e2023JD040227. https://doi.org/10.1029/2023JD040227

Received 16 OCT 2023
Accepted 15 AUG 2024

Abstract This study uses a unique combination of geostationary and low-Earth orbiting satellite-based lightning and precipitation observations, respectively, to examine the evolution of deep convection during the tropical cyclone (TC) lifecycle. The study spans the 2018–2021 Atlantic Basin hurricane seasons and is unique as it provides the first known analysis of total lightning (intra-cloud and cloud-to-ground) observed in TCs through their extratropical transition and post-tropical cyclone (PTC) phases. We consider the TC lifecycle stage, geographic location (e.g., land, coast, and ocean), shear strength, and quadrant relative to the storm motion and environmental shear vectors. Total lightning maxima are found in the forward right quadrant relative to storm motion and downshear of the TC center, consistent with previous studies using mainly cloud-to-ground lightning. Increasing environmental shear focuses the lightning maxima to the downshear right quadrant with respect to the shear vector in tropical storm phases. Vertical profiles of radar reflectivity from the Global Precipitation Measurement mission show that super-electrically active convective precipitation features (>75 flashes) within the PTC phase of TCs have deeper mixed phase depths and higher reflectivity at −10°C than other phases, indicating the presence of more intense convection. Differences in the net convective behavior observed throughout TC evolution manifest in both the TC-scale frequency of lightning-producing cells and the intensity variations amongst individual convective cells. The combination of continuous lightning observations and precipitation snapshots improves our understanding of convective-scale processes in TCs, especially in PTC phases, as they traverse the tropics and mid-latitudes.

Plain Language Summary Tropical cyclones (TCs) are a global weather phenomenon that can cause significant damage, especially to densely populated coastal regions. TCs are characterized by convective elements that produce intense precipitation and sometimes grow strong enough to produce lightning. However, little is known about convective attributes of TCs as they traverse the mid-latitudes and undergo extratropical transition. This study uses new satellite observations of the mid-latitudes to examine how the nature of convection changes throughout the TC lifestyle. Satellite-observed total lightning (cloud-to-ground + intra-cloud) maxima in tropical storms primarily occur on their right side of the storm motion vector and downshear of their center. Differences in environmental shear shift the observed lightning maxima during the tropical storm phase and play a larger role in precipitation distribution than motion. Satellite-based radar observations indicate that electrically active convective precipitation features are deeper, have stronger vertical motions, and more intense rainfall than their non-electrically active counterparts. The results of this study reveal new insights about the distribution and intensity of convective elements within TCs, which could be incorporated into TC assessments and help improve forecasts.

1. Introduction

Tropical cyclones (TCs) form from low-level cyclonic vorticity maxima located in weak wind-shear conditions and are associated with deep convection and heavy precipitation. Latent and sensible heat fluxes from the warm, near-surface layers of the tropical ocean provide these systems energy. TCs that maintain their organization are often steered poleward where they may encounter land or cooler ocean temperatures and interact with increasingly baroclinic environments leading to an extratropical transition (ET). During TC phase changes, the temperature and instability structures of the incipient TC are markedly altered, which in turn affect TC thermodynamic, microphysical, and kinematic characteristics (i.e., convective character). Hence, we expect to see changes in precipitation and lightning behavior throughout the TC lifecycle, in particular, the ET stage.

Although approximately 50% of Atlantic TCs (Hart & Evans, 2001), 30% of western North Pacific TCs (Klein, 1997; Klein et al., 2000), and 10% of Australian TCs (Foley & Hanstrum, 1994) undergo ET and become post-tropical cyclones (PTCs), knowledge gaps concerning PTC storm structure and processes still remain as many TCs that undergo ET are well removed from the coverage of land-based observational networks (C. Evans et al., 2017). These PTCs are still often associated with extreme precipitation, high winds, and can cause loss of life and property around the globe (Blake et al., 2013; Meltzer et al., 2021; Roy et al., 2022; Sainsbury et al., 2020; Stewart, 2018). Therefore, it is important to characterize PTC storm and precipitation structures to acquire a more complete understanding of kinematic and thermodynamic processes occurring throughout the TC lifecycle. In turn, a more complete understanding and characterization of TC lifecycle phases and associated storm structure will lead to improved warning decision support and numerical weather prediction.

Previous studies have used a variety of both ground- and satellite-based sensors to examine lightning in TCs—the rate of lightning activity being applied herein as a proxy for particularly intense and deep convective intensity. TC studies utilizing ground-based radio networks composed of very low-frequency (VLF) sensors, such as the National Lightning Detection Network (Corbosiero & Molinari, 2002, 2003; Lyons & Keen, 1994; Molinari et al., 1994, 1999; Samsury & Orville, 1994), very-high frequency sensors, such as the Los Alamos National Laboratory's Sferic Array (Fierro et al., 2011; Shao et al., 2006), or lightning mapping arrays (Griffin et al., 2014; Logan, 2021) are typically confined to a ∼500 km (or less) buffer of the U.S coast. Such networks have supplemented other data sets when observing TC lightning (Fierro et al., 2011; Hu et al., 2020; Shao et al., 2005). Meanwhile, other TC studies utilize networks such as the World Wide Lightning Location Network (Abarca et al., 2011; DeMaria et al., 2012; Pan et al., 2010; Stevenson et al., 2014, 2016; Wang et al., 2016, 2018; W. Zhang et al., 2015) composed of globally distributed VLF sensors. Though these networks do not perform exactly the same, they primarily detect cloud-to-ground (CG) and some higher peak current intra-cloud (IC) lightning, which is an incomplete depiction of total lightning flash rates (CG + IC) that are needed to provide a better, physically-integrated indicator of convective lifecycle dynamics and vigor (Carey & Rutledge, 1996; Deierling & Petersen, 2008; Goodman et al., 1988; Schultz et al., 2011). TC lightning is frequent in the inner core/eyewall region and can be even more frequent in the outer rainbands (Abarca et al., 2011; Fierro et al., 2018; Molinari et al., 1999; Stevenson et al., 2016; Wang et al., 2018; Xu et al., 2017). Additionally, previous studies utilizing ground-based lightning observations show that there tends to be more lightning detected during weaker TC phases (DeMaria et al., 2012; W. Zhang et al., 2015).

Satellite-based optical lightning sensors onboard low-Earth orbiting (LEO) satellites such as the Optical Transient Detector (Christian et al., 2003) and the Lightning Imaging Sensor (LIS) on the Tropical Rainfall Measuring Mission (TRMM; see Table A1 in Appendix A for acronym list) satellite (Christian et al., 1992) have provided the opportunity to collect many TC samples within the global tropics, build up TC climatologies, and perform statistical studies on TC lightning evolution (Cecil et al., 2002; Cecil & Zipser, 1999, 2002; Jiang et al., 2013; Xu et al., 2017). However, the short duration snapshots afforded by LEO satellites do not allow a temporally continuous analysis of electrical activity for individual TCs. More recent satellite-based lightning observations including those from the Geostationary Lightning Mappers (GLMs; Goodman et al., 2013; Rudlosky et al., 2019; Rudlosky & Virts, 2021) onboard the GOES-16,-17, and −18 satellites enable us to observe total TC lightning trends as these systems develop, evolve, and undergo ET, primarily ≥35° latitude (Hart & Evans, 2001), a region not well-sampled by TRMM-LIS. Alternatively, while providing temporally continuous lightning and convective cloud top observations, geostationary satellites do not provide specific samples of collocated vertical profiles of convective precipitation structure. The microwave sensors onboard TRMM have provided insights into TC vertical precipitation structure (Fritz et al., 2016; Hence & Houze, 2011, 2012) as well as electrical, kinematic, and microphysical processes during the TC lifecycle equatorward of 35° (Cecil et al., 2002; Cecil & Zipser, 2002; Jiang et al., 2011, 2013; Jiang & Ramirez, 2013; Tao et al., 2017; Tao & Jiang, 2015). As a result of the creation of a TRMM precipitation feature (PF) database (Liu et al., 2008) and the resultant TRMM PF research methodology (Jiang et al., 2011; Liu et al., 2011; Nesbitt et al., 2000), a similar approach has been recently extended into the Global Precipitation Measurement (GPM) and GLM era and been used to examine the precipitation and lightning characteristics of mid-latitude systems (Heuscher et al., 2022).

Recent studies have used GLM-proxy data (Stevenson et al., 2018) or GLM data in comparison to ground-based networks (Fierro et al., 2018; Hu et al., 2020; Ringhausen & Bitzer, 2021) to gain further understanding of TC processes on convective timescales. These studies, spatially limited due to ground-network detection efficiency (DE), emphasize how the temporally continuous GLM lightning observations provide the opportunity to further

address lingering questions about lightning occurrence and significance (and by proxy, convection) in TCs. Including GLM observations in the GPM PF database enables a new capability to temporally resolve the electrical evolution of individual TCs, which can be used as a proxy for understanding changes in convective processes. Accordingly, this study is the first to combine continuous lightning observations from GLM with discrete instantaneous precipitation samples (e.g., feature "snapshots") from GPM to help elucidate the behavior of convection and lightning through the entire TC lifecycle from the tropics to the mid-latitudes.

2. Data and Methodology

2.1. Lightning Data

Lightning data collected from the GOES-16 GLM is used in this study. GLM ground sample distance varies from ∼8 km at nadir to ∼14 km at the edges of its field of view (FOV), which spans roughly 137°W to 15°W, 57°S to 57° N. The mean daily GLM flash DE has been shown to be ∼75% (D. Zhang & Cummins, 2020), is higher at night, decreases significantly near the FOV edges, and can be reduced for flashes that occur at low altitudes within optically thick clouds (Bateman & Mach, 2020; Marchand et al., 2019; Rudlosky & Virts, 2021; Rutledge et al., 2020). This study utilizes GLM flash data that has been declared both provisional (Provisional Validation was 19 January 2018) and fully validated (Full Validation was 1 November 2018). To mitigate decreased data quality, only GLM flashes with a quality flag = 0 are used in this study (Carlomusto, 2019; Rudlosky et al., 2019; Rudlosky & Virts, 2021). Due to the DE decrease near the FOV edges, only data occurring between 0° and 57°N latitude and 110°W to 14°W longitudes are used in this study.

2.2. GPM Precipitation Features (PFs)

The GPM mission consists of a constellation of LEO satellites that collectively provides global precipitation maps on an approximately 3-hourly temporal scale (Hou et al., 2014). These satellites carry microwave instrumentation at frequencies spanning 10-183-GHz, which are sensitive to different sizes and phases of precipitation particles distributed throughout the atmospheric column. The GPM Core Observatory (GPM-CO) carries the Dual-frequency Precipitation Radar (DPR), effectively two radars operating at the Ku- (13.5-GHz) and Ka- (35.5-GHz) bands (Iguchi et al., 2003), and the multi-channel GPM microwave imager (GMI; Hou et al., 2014).

Similar to the approach used for creating the TRMM PF database (Liu et al., 2008), GPM PFs are defined for Ku-band radar-derived near-surface precipitation rates >0.1 mm hr^{-1} (rPFs) and contiguous Ku-band radar pixels defined as convective precipitation (cPFs). Since TCs may go unsampled by the GPM DPR for several days due to overpass frequency and a relatively narrow DPR swath, PFs derived from GMI brightness temperatures (T_B) with precipitation rates >0.1 mm hr^{-1} are also used herein (1CPFs). Due to similar footprint sizes at 89-GHz, 1CPFs are also derived from the AMSR2 instrument onboard the GCOM-W1 satellite (Kasahara et al., 2012; Oki et al., 2010) to increase samples. Although previous studies have examined TCs utilizing multi-platform passive microwave observations (Alvey et al., 2015; Cecil & Zipser, 1999), this study is the first to do so in the combined GLM and GPM era. Following Heuscher et al. (2022), GLM lightning observations within ±10 min of the GPM-CO or GCOM-W1 overpass are incorporated into the 1CPFs to define those features as electrically active or non-electrically active. The cPFs represent discrete convective regions within larger precipitation systems (e.g., we interchange "cPF" with "cell"—acknowledging that they are not necessarily exactly the same) associated with rPFs, although not all rPFs have convective rain. Additionally, cPFs and rPFs may be associated with 1CPFs in a similar manner due to the different PF definitions.

2.3. TC Data and Classification

North Atlantic Basin TC best-track observations for the 2018–2021 seasons are obtained from the National Hurricane Center (Landsea & Franklin, 2013) via the International Best Track Archive for Climate Stewardship (IBTrACS; Knapp et al., 2018; Knapp & Kruk, 2010), version 4. Within IBTrACS, 6-hourly position information is temporally interpolated to 3-hourly individual time periods (ITPs) using splines. Parameters not related to position (e.g., maximum sustained wind speed (MSW) and minimum sea level pressure (MSLP)) are linearly interpolated (Knapp, 2019). Position uncertainty included in such data sets generally decreases with increasing intensity (Torn & Snyder, 2012). Information on the tropical storm force wind radius (TSR) and the radius of maximum winds (RMW) is also available for each ITP, which is used extensively in this study. Eyewall convection is collocated with the RMW due to radial convergence, an increased tangential wind speed, and a sudden

upward turning of air within the RMW (Houze, 2010; Rogers et al., 2016). A 5 km buffer is added to the RMW to account for sloped eyewalls (Hazelton & Hart, 2013; Jorgensen, 1984; Rogers et al., 2012; Shea & Gray, 1973; Stern & Nolan, 2009). The TSR used is the mean of the 34-knot wind within each quadrant. If no RMW (TSR) value is present, a value of 80 (120) km is used for tropical ITPs. The 80 km RMW value, used in 8% of ITPs, was chosen as it is roughly the 75th percentile of Atlantic Basin TC RMWs from 1988 to 2002 (Kimball & Mulekar, 2004). This 80 km distance from the TC center is approximately where previous lightning studies have observed a lightning minima between the inner core and outer rainbands (Cecil et al., 2002; Corbosiero & Molinari, 2002, 2003; Molinari et al., 1994, 1999; Squires & Businger, 2008). The climatological mean TSR found within the Atlantic Basin from 1988 to 2004 has been shown to range from 107 to 225 km depending on the number of samples (Kimball & Mulekar, 2004; Knaff et al., 2007). Herein, a TSR value of 120 km was used in 34% of ITPs to align with Knaff et al. (2007), due to their larger sample size (and possibly more diverse environmental conditions). For ITPs classified as PTCs, a value of 150 (220) km was utilized for the RMW (TSR); even though no climatological analyses of PTCs have been undertaken, this RMW is within the RMW range observed in TC Bonnie (1998) after it underwent ET (C. Evans & Hart, 2008).

To enable comparisons with previous studies, this study utilizes the 3-hourly ITPs available in IBTrACS, occurring at either main or intermediate synoptic times. Because a focus of this study is to look at the PTC phase (i.e., after ET), which may not always be included in the NHC best-track data, the best-track positions are extended by tracking MSLP minima and vorticity (Hodges & Emerton, 2015; Serra et al., 2010) in the fifth-generation European Center for Medium-Range Weather Forecasts (ECMWF) global atmospheric reanalysis (ERA5; Hersbach et al., 2020). ERA5 has a $0.25° \times 0.25°$ horizontal grid spacing, is available in hourly time steps, has been used to track TCs and extratropical cyclones using either vorticity alone (Gramcianinov et al., 2020) or a vorticity and MSLP combination (Zhong et al., 2023), and is able to depict TC and PTC structure (Bian et al., 2021; Dullaart et al., 2020; Malakar et al., 2020; Sarro & Evans, 2022). Track extension is performed similar to Hodges and Emerton (2015) with the vorticity at the 850-, 700-, and 600-hPa levels being vertically averaged. The MSLP minima location within a 4° box centered on the previous location is selected as the new location if the vertically averaged vorticity exceeds a threshold of 5×10^{-6} s^{-1} (Hodges & Emerton, 2015) to help eliminate existing extratropical low-pressure systems. Additionally, if two subsequent steps in the extended track are at the same latitude/longitude pair, the track is ended at the first of these steps, reducing the extension of weaker systems.

Based on the 1-min MSW, ITPs are classified into life-cycle phase. Classifications include tropical storms (TS; $34 \leq \text{MSW} \leq 63$ kt), category 1 or 2 hurricanes (CAT12; $64 \leq \text{MSW} < 95$ kt), category 3 to 5 hurricanes (CAT35, MSW ≥ 95 kt), and post-tropical cyclones (PTC; classified based on an asymmetry factor, B). B measures the symmetry shift in the thickness field, resulting from low-level frontogenesis and increasing baroclinicity (J. L. Evans & Hart, 2003; Hart, 2003) and is calculated via:

$$\boldsymbol{B} = \boldsymbol{h}\left[\overline{(\boldsymbol{Z_{600}} - \boldsymbol{Z_{900}})}_{\boldsymbol{R}} - \overline{(\boldsymbol{Z_{600}} - \boldsymbol{Z_{900}})}_{\boldsymbol{L}}\right] \quad (1)$$

where h indicates the hemisphere and is positive for the Northern Hemisphere. The overbar is the areal mean (within 500 km) over the semicircle with respect to storm motion of the thickness field. Similar to J. L. Evans and Hart (2003), ET onset is defined to be where $|B| > 10$ m; however, this study requires two consecutive ITPs after the IBTrACS minimum pressure with $|B| > 10$ and ET onset is defined as the first of these two ITPs. It is also assumed that the system remains post-tropical after onset.

Lightning flashes and PFs are collocated with storm ITPs if they are within the 3 hours following the ITP start time and are within 2*TSR. As storms can often grow in size during the ET stage, using the default TSR value of 220 km could limit the amount of lightning/PFs collocated with the storm in these ITPs. This will cause the results presented herein to be *low* estimates within PTC stages (cf. Tables 2 and 3). ITPs are not used if the storm center for a particular ITP is outside the GLM FOV. Resulting ITP counts are listed in Table 1, with TS and PTC ITPs each having more than 1,200 samples and CAT12 (CAT35) hurricanes having approximately 500 (300) samples. For results broken down by TC phase, the two ITPs immediately following when a TC transitions phase are removed to ensure that the results fully represent that phase (i.e., if a TC transitions from a TS to a CAT12, the 6 hr immediately following the transition at the CAT12 phase are removed). PFs are constrained to having all their constituent pixels reside entirely within the GLM FOV. Similar to the conservative approach of Heuscher et al. (2022), features were also removed if they were not fully within the DPR (GMI/GCOM-W1) scan for cPFs and rPFs (1CPFs).

Table 1
Number of 3-Hourly ITPs Within Each TC Phase Considered in This Study Without (With) Transitional ITPs Removed

	TS (34 ≤ MSW ≤ 63 kt)	CAT12 (64 ≤ MSW < 95 kt)	CAT35 (MSW ≥ 95 kt)	PTC (asymmetry factor)
2018	513 (459)	171 (143)	45 (39)	272 (260)
2019	413 (367)	95 (75)	80 (72)	172 (160)
2020	721 (637)	188 (143)	66 (51)	448 (428)
2021	375 (315)	85 (62)	104 (96)	320 (308)
Total	2,022 (1,778)	539 (423)	295 (258)	1,212 (1,156)

Following Corbosiero and Molinari (2002, 2003; hereafter CM02/CM03) and Matyas (2010), TCs are partitioned into motion-relative and shear-relative quadrants with the motion and shear vectors aligned to a northward-directed reference frame. This results in forward motion and downshear quadrants being located to the north of the storm center (cf. Matyas, 2010, Figure 2). Angles relative to the shear and motion vectors are calculated for lightning and PF locations as well as an RMW-scaled distance, r^*, from the TC center via:

$$r^* = \frac{r}{\mathbf{RMW}} \tag{2}$$

with r being the distance from the TC center [km]. This RMW-normalized compositing scheme is used to dynamically account for differing TC sizes. Due to differing RMWs for TC phases, r^* for different strengths are not necessarily equal (i.e., $TS_{r^*} \neq CAT12_{r^*}$). For reference, in hurricanes, 1–2 r^* roughly corresponds to the primary eyewall location, whereas 2–3 r^* corresponds to rainbands and secondary eyewalls (DeHart et al., 2014; Rogers et al., 2012). An additional caveat with using an r^* value for PTC ITPs is that these systems start to become less symmetric as they start to develop fronts; some of these asymmetric features may be lost when analyzed within an r^* framework. Following W. Zhang et al. (2015) and Yang et al. (2020), the environmental vertical wind shear for each ITP is calculated by averaging the ERA5 850-hPa and 200-hPa 3-hourly horizontal wind vectors over a 200–800 km radius from the TC center in order to remove the TC circulation center. As the best-track centers are used for shear calculations, errors may arise if the best-track center is different than the TC center within reanalysis.

3. Results

3.1. GLM Observations

A total of 3,321,778 lightning flashes were detected by GLM in the 88 TCs and associated phases observed during the 2018–2021 Atlantic hurricane seasons; if transitional ITPs are removed, a total of 2,517,715 flashes are observed (Table 2). A total of 55 TCs (62.5%) completed ET, a larger sample fraction than previously reported (Hart & Evans, 2001). The results suggest more lightning flashes occur in PTCs than in tropical phases for normalized flash counts, while PTCs and TSs have similar raw flash counts. Higher normalized flash counts may be influenced by larger areas during the PTC phase, the higher probability of PTC ITPs being over land where lightning activity is generally more frequent than over ocean (Boccippio et al., 2000; Williams & Stanfill, 2002), increased ice-phase processes in baroclinic environments, and slightly more TS ITPs (Table 1). We note that although extensions of weaker extratropical system tracks should be reduced (Section 2.3), the inclusion of these weaker tracks may slightly increase the amount of lightning observed within the system, but overall trends should be similar. To account for the continental influence on landfalling TCs (May et al., 2008; Morin & Parker, 2011; Schenkel et al., 2023; Slocum et al., 2023), ITPs are classified as oceanic (continental) if less than 40% (more than 60%) of the latitude/longitude pairs within 2*TSR are over land. Subsequent analysis presented in this study is from oceanic and continental ITPs combined as separating these ITPs demonstrates similar results.

We also find that CAT35 major hurricanes phases typically contain less lightning than other TC phases, consistent with previous studies (Cecil & Zipser, 1999; DeMaria et al., 2012; W. Zhang et al., 2015). A few reasons for this lightning frequency difference are the occurrence of fewer CAT35 ITPs (Table 1) which are typically oceanic (Figure 1a) where less lightning occurs when compared to continents. Additionally, while lightning has been

Table 2
Lightning Statistical Measures by TC Phase

	TS	CAT12	CAT35	PTC
Flash Count				
Total	1,118,280	184,427	109,705	1,105,303
Continental ITPs	19,197	346	21	387,362
Oceanic ITPs	1,069,170	153,816	103,530	605,070
Percentage of Total Flashes				
Continental ITPs	1.7%	0.2%	0.02%	35%
Oceanic ITPs	95.6%	83.4%	94.4%	54.7%
Flashes/ITP [fl 3 hr^{-1}]				
Total	628.9	435.9	425.2	956.1
Continental ITPs	102.6	10.2	1.75	1,384.2
Oceanic ITPs	649.5	341.1	393.7	720.5
Mean (95th percentile)	5.1 (26.4)	3.9 (17.4)	4.1 (13.9)	4.3 (21.9)
Flash Rate [fl min^{-1}]				

Note. See text for continental/oceanic ITP definitions.

Table 3
PF Counts by TC Phase

	TS	CAT12	CAT35	PTC
Total Count				
1CPF	6,026	2,550	1,667	8,718
rPF	2,521	1,213	667	2,447
cPF	3,080	1,408	959	1,977
EA Count				
1CPF	108	36	62	25
rPF	50	35	31	7
cPF	105	48	52	12
super-EA Count				
1CPF	20	9	10	2
rPF	2	2	2	0
cPF	4	2	4	2
Mean Area [km^2]				
1CPF	16,291.4	16,446.4	12,860.3	9,654.6
rPF	2,444.4	2,966.4	2,629.6	2,388.2
cPF	426.9	361.0	391.8	383.6

associated with hurricane intensification (Fierro et al., 2011; Molinari et al., 1994, 1999; Squires & Businger, 2008; Stevenson et al., 2016), major hurricanes have a lower chance of increasing intensity on the Saffir-Simpson classification scale. TS and PTC phases have larger mean and 95th percentile flash rates, a common storm intensity metric, than hurricane phases. More lightning flashes in the TS/PTC phases combined with similar *mean* flash rates to hurricane phases but higher *extreme* flash rates suggests that convection within TCs is driven by a balance of storm-scale convective frequency (inferred by the number of lightning flashes) and convective intensity (e.g., flash rate). This balance between lightning frequency and convective intensity has been previously seen when looking at lightning land/ocean contrasts as well as the diurnal timescale (Boccippio et al., 2000; Williams et al., 2000).

Lightning flashes in all, TS, and PTC phases exhibit a unimodal distribution whereas a slight bimodal distribution is observed for hurricane phases, with large inter-storm variability (Figure 2). The radial distributions of lightning partitioned by TC phase add more insight into the source of bimodal radial lightning distributions reported in previous TC studies that included multiple TC phases in a single distribution (Abarca et al., 2011; Cecil et al., 2002; Molinari et al., 1999; Stevenson et al., 2016; Xu et al., 2017). A bimodal lightning distribution in hurricane phases might be expected due to updraft strength differences between the eyewall (1–2 r^*) and rainband regions (2–3 r^*). Stronger updrafts, observed in eyewalls when compared to rainbands (Black et al., 1996; Jorgensen et al., 1985), can lead to more turbulence as well as loft more hydrometeors into the mixed phase region, supporting more frequent flashes (Bruning & MacGorman, 2013; Carey et al., 2019; Deierling & Petersen, 2008). These strong eyewall updrafts, while extending through the troposphere (Black et al., 1996), maximize around 8-km altitude (Lord et al., 1984; Marks & Houze, 1987), well within the mixed phase zone for this study. One might also see a greater influence on TC convection in the rainband regions due to environmental inhomogeneities (e.g., sea surface temperature gradients, conditional instability/aerosol gradients, underlying surface inhomogeneities, fronts/jets, etc.,) whereas TC inner-core convection is more strongly driven by TC dynamics that interact with relatively small perturbations in mixed layer thermodynamic properties. The lack of a bimodal distribution in total flashes may be due to our storm compositing, the inclusion of ITPs after ET onset, and the observation of temporally continuous total lightning from GLM.

Figure 3 shows the motion and shear relative lightning within analyzed ITPs. The GLM data indicate that TC lightning flashes tend to mostly occur on the forward right flank as well as downshear of the TC center (Figures 3a and 3b). Motion and shear relative lightning distributions correspond to the unimodal radial distribution for all flashes observed in Figure 2a, with the peak 1–3 r^* from the TC center. To remove TC duration bias from this lightning analysis, Figures 3c and 3d show the flash count per ITP, which can be interpreted similar to a three-hour average flash rate. The flash rates show lightning maxima in the back left quadrant, approximately 1–2 r^* from the center (Figures 3a and 3c). The lightning maxima in the forward quadrants and the back left quadrant are similar (Figure 3a), but flash rates are lower in forward quadrants (Figure 3c) due to more ITPs contributing to the overall flash count in those quadrants. More frequent flashes are in the downshear right quadrant approximately 1–2 r^* from the TC center, similarly collocated with flash count maxima (Figures 3b and 3d) and the unimodal radial distribution (Figure 2a). The region between 1 and 2 r^* from the TC center aligns with the strongest updrafts (Black et al., 1996; Jorgensen et al., 1985). Additionally, lightning could be more widely distributed within this region due to tilted eyewall convection with cloud tops where lightning is located being radially removed

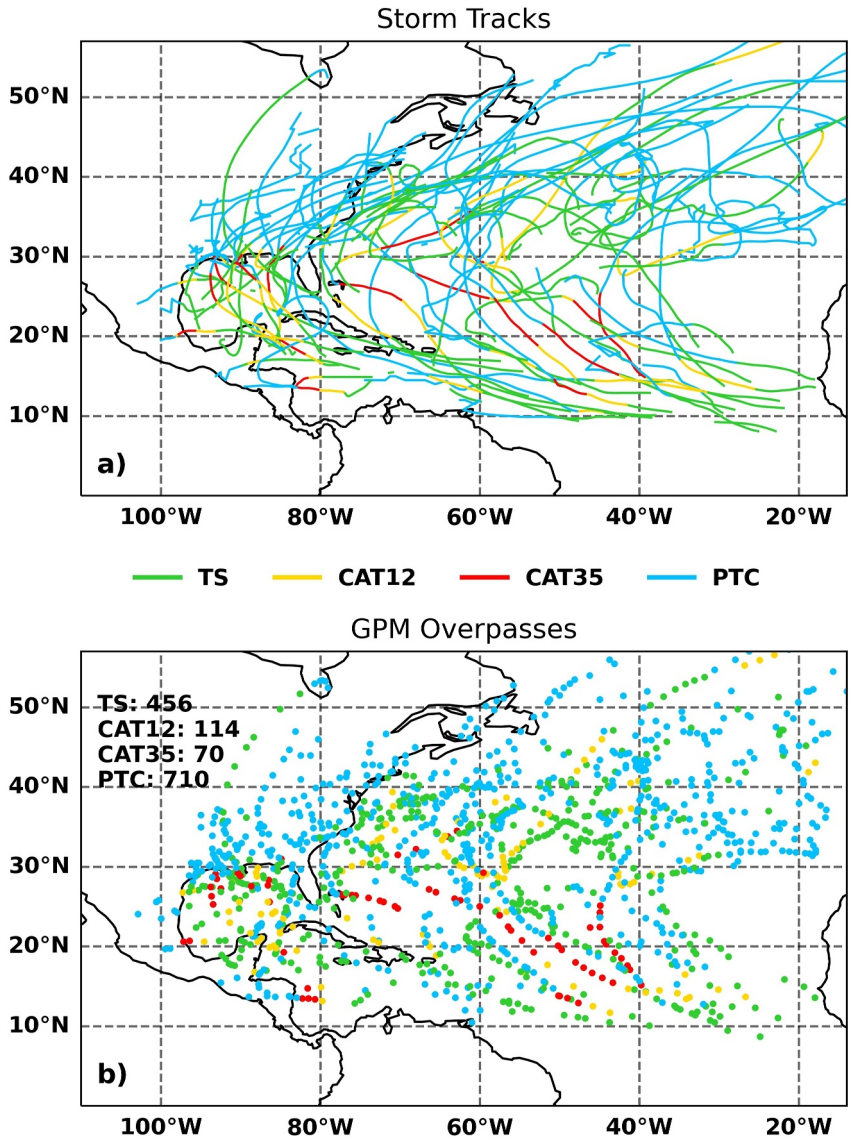

Figure 1. TC tracks from the 2018–2021 Atlantic Basin hurricane seasons within the GLM FOV (a) and associated GPM mission overpasses for each phase used in this study (b).

from the RMW, which occurs at low altitudes. Pockets of higher flash rates occur downshear, approximately 4–5 r^* from the TC center, which may be indicative of convection occurring in the TC outer rainbands.

To prevent prolific lightning-producing TCs from dominating the flash count distribution the preferred lightning quadrant for each ITP is calculated. Similar to CM02/CM03, the preferred lightning quadrant for each ITP is defined as the quadrant with the most flashes during that ITP. Figure 4 shows the GLM-observed lightning maxima is located on forward right side (Figure 4a) and downshear (Figure 4b), consistent with previous studies (cf. CM03's Figure 1). As the downshear right quadrant count in this study exceeds the downshear left quadrant by two ITPs, the marker for all ITPs (blue star in Figure 4b) is placed on the shear vector and the maxima is described as "downshear" as opposed to either right or left of the shear vector. Similar results are obtained when TC phase is separated, if the ITP time is centered (i.e., lightning flashes from 1030 UTC to 1330 UTC are associated with an ITP time of 1200 UTC), and for ITPs constrained to GPM overpass occurrences.

Several key differences between this and previous studies in Figure 4 should be noted. First, previous studies included in Figure 4 use either ground-based lightning detection networks (Abarca et al., 2011) or ground-based radar reflectivity (Matyas, 2010), which do not necessarily capture the vertical precipitation distribution and the

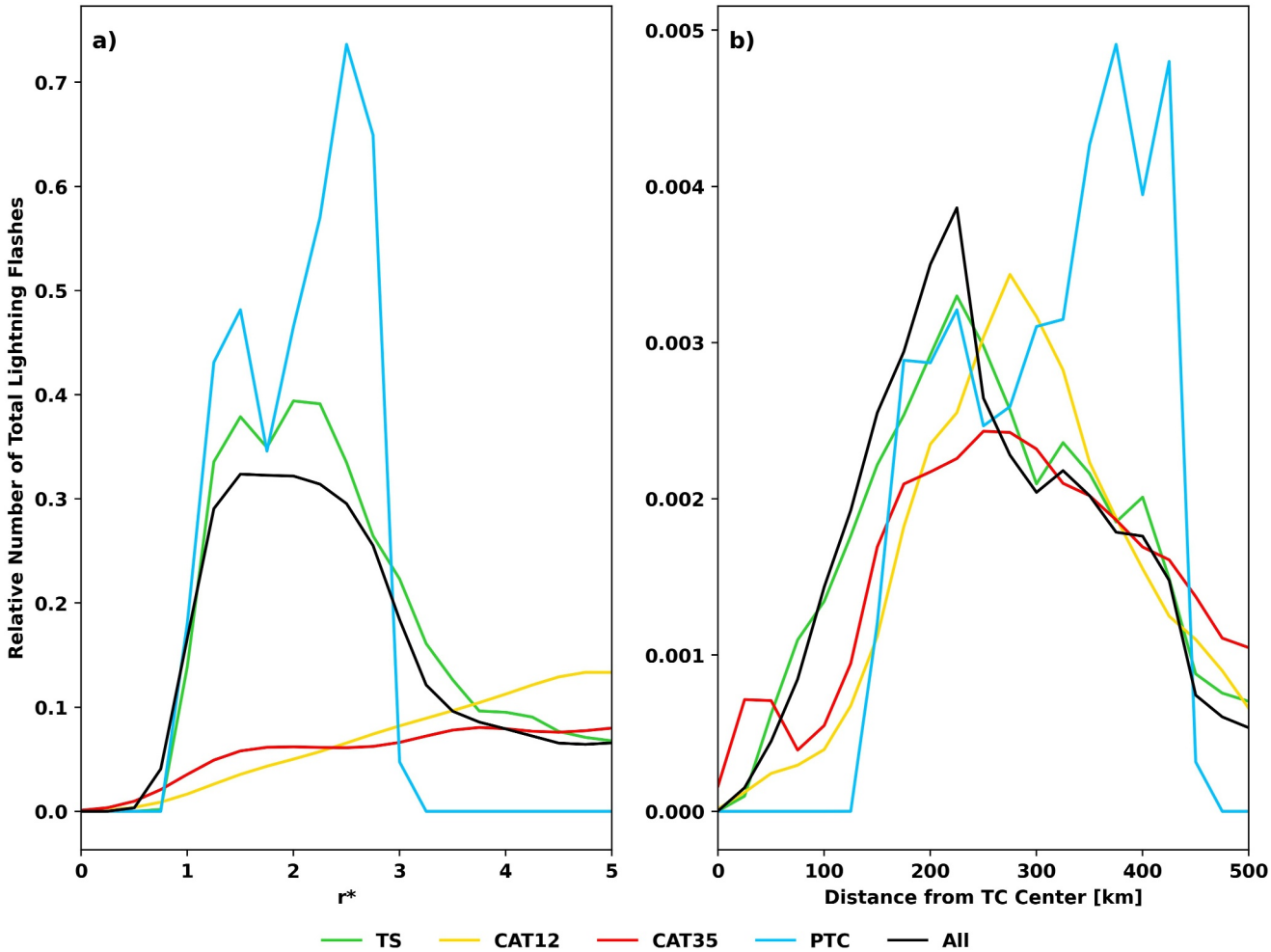

Figure 2. Radial distributions of the normalized (panel a) and actual (panel b) distance from the TC center for all lightning flashes, as well as by TC phase.

total lightning flash count. Fierro et al. (2018) uses GLM lightning data, but only a single 72-hr period during Hurricane Maria (2017). Previous studies also look at the lightning max in the inner core/outer rainband regions, whereas this study does not differentiate these spatial regions. The shear relative plot shows that most other studies find one maximum to the left and another maximum to the right of the shear vector (e.g., CM02/03 for the inner core and outer rainband maximum respectively). If both maxima for CM02/03 are combined, a downshear right maximum is observed, consistent with this study. It should be noted that CM02/03 does not separate out PTC phases, but uses tropical depression, TS, and hurricane phases. Furthermore, although CM02/03 separate out pre- and post-landfall observations into separate ITPs, post-landfall ITPs, which could be a proxy for PTC phases, are not analyzed separately.

The results from this study support previously developed conceptual models of TC structure (Hence & Houze, 2012). In these models, convection initiates downshear right and intensifies as it rotates counterclockwise to the downshear left quadrant. Figures 3b and 3d show that the downshear right quadrant has the most lightning flashes and highest flash rates respectively, followed by the downshear left quadrant. This is consistent with convective cell initiation (growth and intensification) in the downshear right (left) quadrant. While one may expect more lightning during the convective growth/intensification stage (e.g., the downshear left quadrant), these convective stages can be characterized by taller clouds and deeper cloud optical depths, resulting in a reduced GLM DE (Marchand et al., 2019; Rutledge et al., 2020). Figure 4b shows that these quadrants are the preferred GLM lightning quadrant for all ITPs, as well as PTC ITPs. Figures 3b and 4b also support previous modeling studies (Frank & Ritchie, 2001), where the preferred region for low-level convergence (and hence positive vertical velocities) due to differential vorticity advection with height is downshear of the TC center.

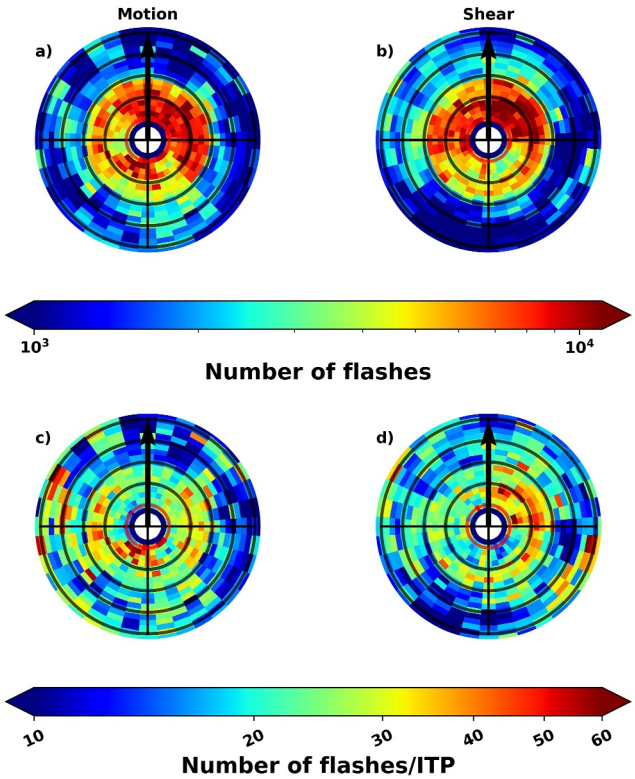

Figure 3. Motion relative (panels a, c) and shear relative (panels b, d) locations for GLM flash counts (0.25 *r**, 10° bins; panels (a, b) and flash rate (0.25 *r**, 10° bins; panels (c, d). Arrows indicate motion/shear vector direction. The red ring represents 1 *r**, with successive *r** values represented by black rings.

These positive vertical velocities help support convective initiation and growth, which can be inferred through lightning observations, in the downshear quadrants.

The vertical wind shear influence on TC lightning is further analyzed by breaking TCs into ITPs characterized by weak (<5 m s^{-1}), moderate (5–10 m s^{-1}), and strong shear (>10 m s^{-1}) (Corbosiero & Molinari, 2002, 2003; Matyas, 2010; Wang et al., 2018). To account for sampling duration differences, normalized flash counts are plotted as a function of shear for TS and PTC phases (Figure 5). Lightning maxima are found in the downshear right quadrants for TS ITPs (Figures 5a, 5c, and 5e). For PTC ITPs, shear tends to have a broad radial distribution of lightning flashes regardless of strength, similar to TS ITPs in weak shear (Figure 5a). Moderate shear tends to focus the lightning flashes in the downshear right quadrant for TS ITPs (Figure 5c). Similar results for PTC radial distributions (e.g., blue line in Figure 2) and motion/shear relative lightning distributions (Figures 4 and 5) are observed if a more conservative RMW (TSR) of 80 km (120 km) is utilized for PTC ITPs (not shown).

3.2. PF Precipitation Structure

Collocation of lightning to GPM-derived PFs and coincident vertical profile and column integrated measurements of precipitation therein may provide insights into the relative intensity versus the number of convective cells (as inferred by PFs) occurring within TCs. Only 2.1% of all PFs analyzed in this study are electrically active (EA), although this varies by PF type. Roughly 1.2% of 1CPFs, 1.7% of rPFs, and 2.9% of cPFs are EA (Table 3). EA percentage differences may arise because of precipitation type and different derivation techniques for the PF populations (cf. Section 2.2) resulting in different statistics. Due to swath width differences between the GMI/AMSR2 and DPR, 1CPFs have larger areas than DPR-derived PFs. The rPF and 1CPF populations have similarly low EA percentages since stratiform systems are included in these PFs. Roughly 10% of EA features are classified to be super-electrically active, defined as consisting of more than 75 flashes. Although partially due to ITP sampling (cf., Table 1), a larger fraction of the sample population is found during TS (Table 3) indicating that the EA cPF *frequency* observed in each phase contributes to convective characteristics during different TC lifecycle phases.

To provide a better understanding of the vertical ice mass distribution, contoured frequency by altitude diagrams (CFADs; Yuter & Houze, 1995) are created for TC EA and super-EA pre-ET and post-ET cPFs. CFADs

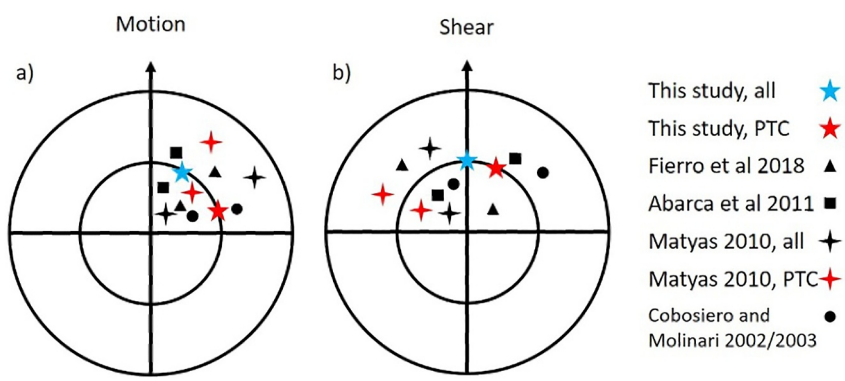

Figure 4. Lightning maxima locations in a motion-relative (a) and shear relative (b) sense for this study compared to previous literature. See text for description of symbol placement. See legend for symbol definitions and references for their data sets/methodologies. Arrows indicate the motion/shear vector direction.

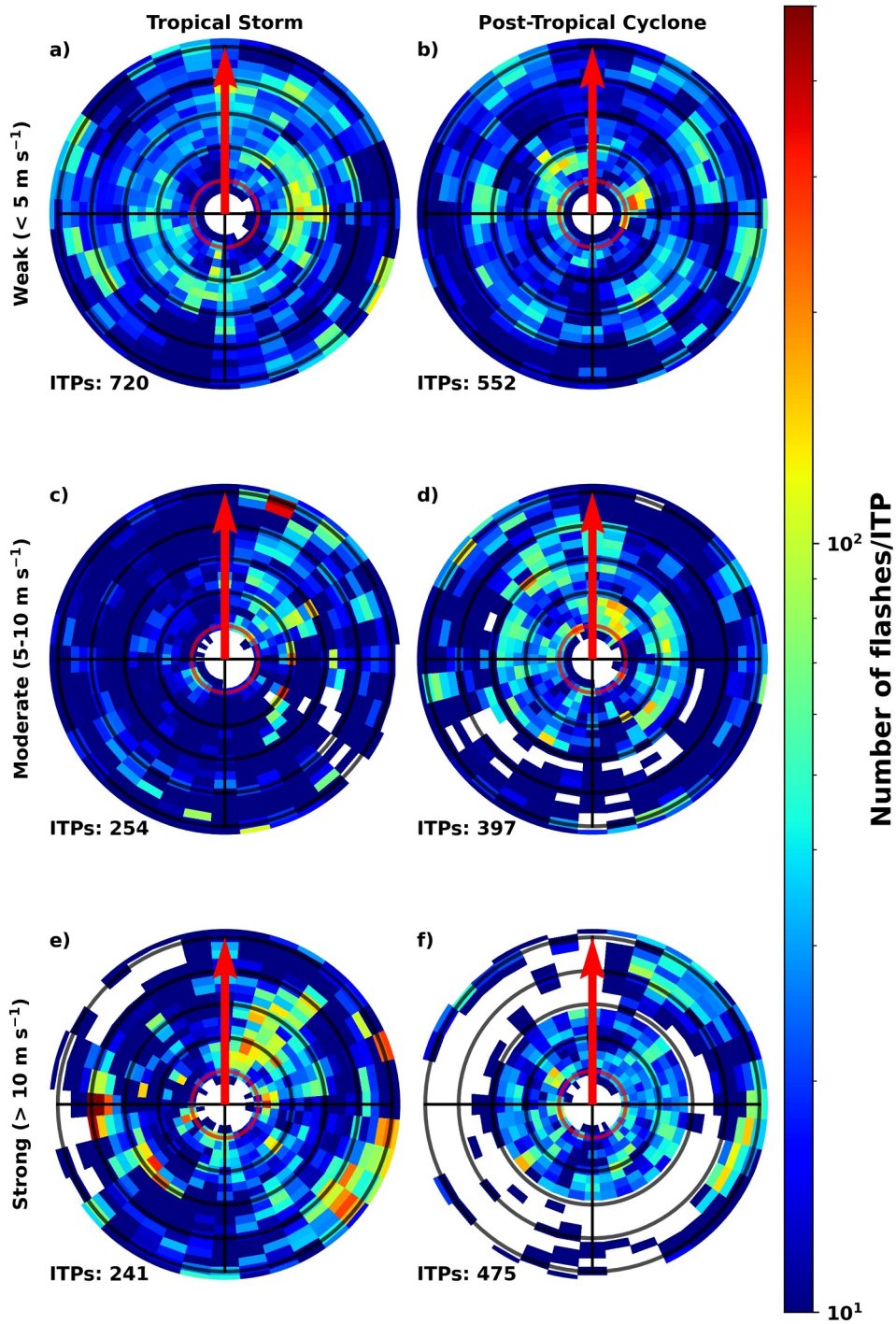

Figure 5. Shear-relative locations for normalized GLM flash counts for weakly sheared (top row), moderately sheared (middle row), and strongly sheared (bottom row) TS (left column) and PTC (right column) ITPs, with ITP counts to the bottom left. Bins, rings, and arrows are as in Figure 3.

(Figure 6) are composed of all Ku-band radar pixels (corrected reflectivity from 2ADPR) within TC-associated cPFs that fall fully within the DPR scan; CFAD distributions are normalized by the absolute maximum sample frequency, similar to Houze et al. (2007), in order to facilitate comparison among the different populations. The mean 0°C, −10°C, and −40°C heights derived from vertical temperature profiles stored in the GPM data sets are also plotted. Post-ET profiles (Figures 6b and 6d) tend to be shorter than pre-ET profiles for both EA and super-

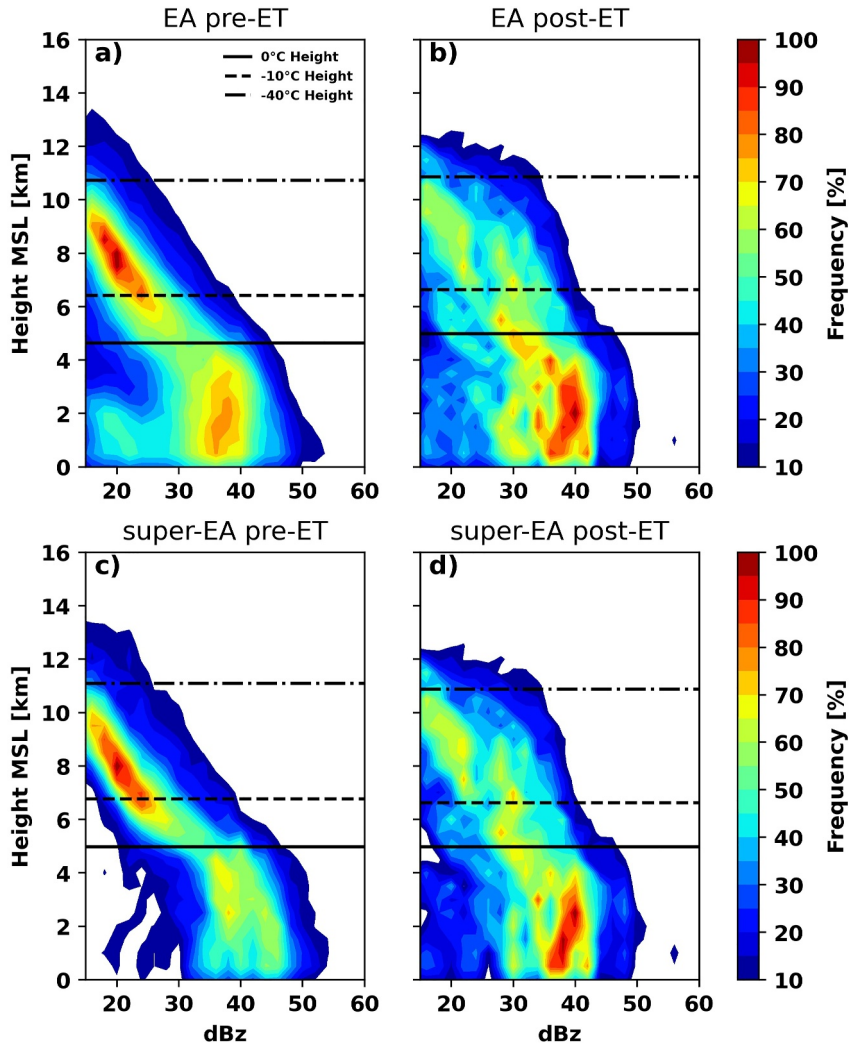

Figure 6. CFADs of GPM Ku-band reflectivity [dBz] for pixels within EA pre-ET (panel a), EA post-ET (panel b), super-EA pre-ET (panel c), and super-EA post-ET (panel d) cPFs.

EA cPFs. Additionally, post-ET EA cPFs have a larger frequency of profiles containing reflectivities below the freezing level, even though the pre-ET profiles have higher maximum surface reflectivities. Although tendencies are hard to compare due to sample size differences, super-EA profiles (Figures 6c and 6d) exhibit a reduced vertical reflectivity gradient relative to EA profiles (i.e., the mode is more vertical, especially in the lower half of the mixed phase zone). Furthermore, the majority of EA profiles (both pre- and post-ET) contain 30 dBz echoes well into the upper mixed phase region. Numerous studies have demonstrated that reflectivity thresholds such as 30–40 dBz at −10°C indicate the presence of ice microphysics conducive to the production of robust storm electrification and associated lightning (Carey & Rutledge, 2000; Dye et al., 1988; Petersen et al., 1996; Zipser & Lutz, 1994). We clearly see these trends in Figure 6, where 10%–15% of the EA cPFs have 40 dBz reflectivity at −10°C and roughly 50% of the super-EA cPFs attain this critical threshold. With more of these "intense" features occurring during the PTC phase (Table 3), it can be implied that the overall convective nature is more intense after a TC undergoes extratropical transition. This more intense convective nature suggests that conditions are more conducive to lightning production after ET completes.

Although radar observations provide a great deal of information for the ensemble of given precipitation profiles and PFs, DPR-derived PFs represent only a small fraction of the PFs sampled due to the narrow DPR swath width as compared to that of the GMI onboard the GPM-CO (Hou et al., 2014) as well as microwave imagers onboard other satellites within the GPM constellation (e.g., AMSR2 onboard GCOM-W1 with a swath width of 1,445 km

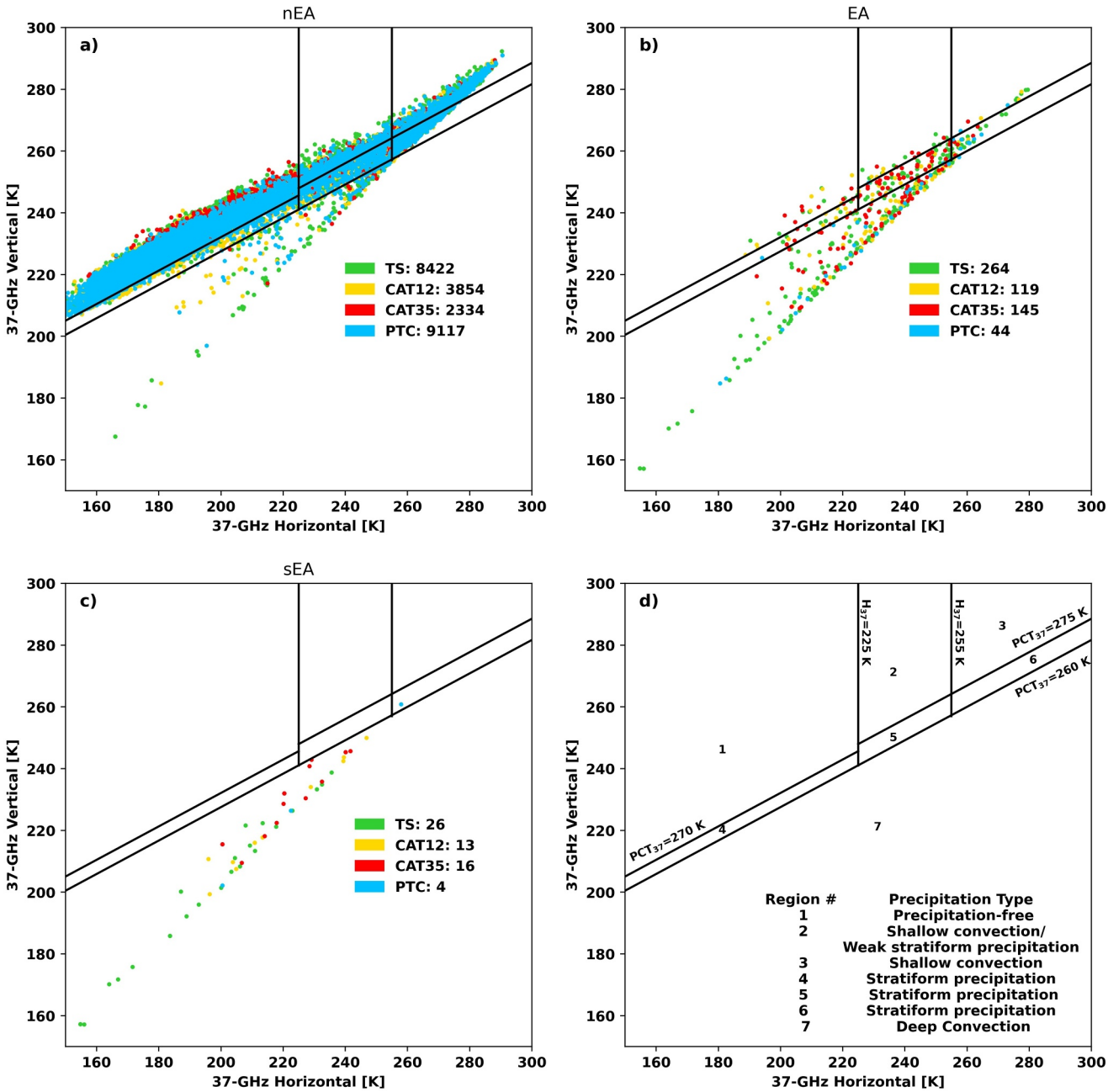

Figure 7. Scatter plots of TC PFs in the NRL 37 color product as defined by J18 and Lee et al. (2002). Points are plotted at the 37_H and 37_V comprising the minimum $PCT_{37\text{-}GHz}$ for (a) non-EA PFs, (b) EA PFs, (c) super-EA PFs. Panel (d) shows the precipitation type associated with each region.

(NASA, 2023)). Thus, we also consider PFs defined from passive microwave observations from both GMI and GCOM-WI (i.e., both cPFs and 1CPFs), which provide more coverage of TCs during overpass events. Using horizontally-polarized 37-GHz (37_H) and vertically-polarized 37-GHz (37_V), Jiang et al. (2018; hereafter J18) and Lee et al. (2002) identified seven different precipitation regimes (cf. Table 2 in J18 or Figure 7d). As numerous 37-GHz pixels may comprise a single PF, we apply the J18 approach to create precipitation region scatterplots partitioned by TC phase for non-EA, EA, and super-EA cPFs (Figures 7a, 7b, and 7c respectively), with each PF being plotted at the 37_H and 37_V representing the minimum polarization corrected temperature at 37-GHz ($PCT_{37\text{-}GHz}$).

Figures 7a and 7b are representative of observed behavior in the CFADs for non-EA and EA cPFs. The non-EA PFs are classified as all 7 types of precipitation, overlapping with EA PFs. The majority of these PFs are classified as

precipitation-free, shallow convection, or stratiform precipitation. Contrasting Figures 7a and 7b, the non-EA PFs classified as deep convection in Figure 7a are likely PFs either just below the threshold of becoming electrically active, or with flashes not detected by the GLM. EA PFs are primarily classified as deep convection (Figure 7b), but all precipitation types are found within EA PFs. This is not unexpected as shallow (or early stage) convection and stratiform precipitation are known to be electrically active (Carey et al., 2005; Dye & Bansemer, 2019; Lang et al., 2004; Rutledge & Petersen, 1994; Schuur & Rutledge, 2000; Stolzenburg et al., 1994). All precipitation types are found within EA PFs due to noise and data/algorithm imperfections. Reasons for non-EA and EA PF overlap (Figures 7a and 7b), as well as the shallow convection classification, may be due to an incorrect assumption that lightning and minimum PCT_{37} are collocated or surface contamination via non-uniform beam filling influencing the observed T_B (Kummerow, 1998) with the large 37-GHz surface footprint (~125 km^2; Hou et al., 2014). Figure 7c shows that super-EA PFs are almost exclusively deep convection, consistent with CFADs from pixels within these PFs (Figure 6c). Figure 7c is also consistent with behavior of the deepest DPR cPF profiles with the higher frequencies of 20 dBz reaching above the mean −40°C level, indicating more integrated ice mass.

4. Summary

New data sets have been created containing merged coincident and spatially-matched satellite observations of cPFs defined from the precipitation profile and column-integrated observations observed by the LEO GPM constellation and temporally continuous geostationary lightning observations from the GOES GLM. These data have been collected over data-sparse, remote locations covering both the tropics and the mid-latitudes, and were used herein for the study of different TC lifecycle phases. The ability to observe and study TCs with continuous observations over tropical and sub-tropical oceans is critical as this is where these systems spend most of their lifetime. Moreover, TCs typically initiate and develop too far from ground-based detection networks to accurately depict their electrical and microphysical evolution. Hence, geostationary satellite-based lightning measurements combined with frequent active/passive microwave observations from LEO satellites offer a unique observational perspective from which to advance our understanding of TCs. Armed with this new merged data set, this study uses observations of four Atlantic Basin hurricane seasons, totaling 88 TCs, to examine coevolving convective structure and lightning behavior in different TC phases. This study is unique in that we specifically characterize lightning observations in TCs that have undergone extratropical transition and have become post-tropical cyclones - a challenging TC phase that has been previously under-sampled and not well studied in the context of precipitation structure and lightning.

The main findings of this study are as follows:

1. The lightning activity radial distribution within TCs is unimodal when all phases are integrated into a single sample. The radial distribution of lightning activity is also unimodal for TS and PTC phases (Figure 2), two TC phases that dominate the TC phase sample space. However, hurricane phases are characterized by bimodal radial distributions of lightning activity consisting of eyewall and outer rainband peaks.
2. When examined in a TC motion-relative (shear-relative) reference frame, lightning flash counts maximize in the forward motion (downshear) direction/quadrants (Figure 3). When looking at preferred lightning quadrants for every ITP, a forward right (downshear) quadrant is found for motion-relative (shear-relative) analysis (Figure 4). Physically this can be explained by convection preferentially occurring within the downshear right quadrant of the TC and intensifying as it rotates counter-clockwise within the TC.
3. Convective differences between TC phases relative to the lightning activity spatial distribution are driven by a balance between the frequency of occurrence of lightning producing cells and intensity differences among them. Tropical storm (TS) and PTC phases exhibit relatively more lightning flashes, higher extreme flash rates, as well as more electrically active (EA) and super-EA cPFs than hurricane phases (Tables 2 and 3). Additionally, vertical profiles of reflectivity from super-EA cPFs during the PTC phase appear to have greater reflectivity at altitudes above the −10°C level than tropical phases, indicating stronger updrafts in cold regions of the convection during this phase. While relatively more intense, the infrequent occurrence of super-EA features results in minimal influence over the EA sample statistics in this study.
4. The addition of passive microwave precipitation classification at 37-GHz (Figure 7) — a means to partition column integrated frozen precipitation behavior weighted more strongly to larger ice hydrometeors — can also help reveal relative presence of electrical activity in TCs, but not necessarily TC phase.

Future research will focus on the addition of more seasons from the Atlantic Basin and expansion to the Pacific Basin, which help will increase TC phase sample numbers, increase the breadth of convective intensities sampled, and further improve the means to characterize physically meaningful differences in lightning and convective structure as a function of ambient environments (e.g., Table 1). Consideration of different ocean basin environments is important because previous research (DeMaria et al., 2012; Stevenson et al., 2016) has indicated that different physical processes may influence TC development in the Atlantic and Pacific Basins. Thus, future research should also focus on TCs in the Pacific Basin using data from the GLMs onboard GOES-17/18, with subsequent comparison to results from the Atlantic Basin to help further isolate the relative occurrence of different physical processes. Analysis of other lightning characteristics observed by the GLM instruments may provide further insight into the inner workings of deep convection associated with TCs and should also be examined. This study suggests the importance of continued, targeted future in-situ microphysical, electrical, and environmental TC observations that encircle the hurricane eye at varying radii to resolve discrepancies in the interpretation of radial distributions of lightning and TC intensification.

Appendix A

Table A1
List of Acronyms Utilized in This Paper

Acronym	Meaning
1CPF	Precipitation feature derived from brightness temperature
CAT12	Category 1–2 hurricane
CAT35	Category 3–5 hurricane
CFAD	Contoured frequency by altitude diagram
CG	Cloud-to-ground
cPF	Radar-derived convective precipitation feature (from the GPM-CO)
DE	Detection efficiency
DPR	Dual-frequency Precipitation Radar
EA	Electrically active
ERA5	European Center for Medium-Range Weather Forecasts (ECMWF) fifth-generation reanalysis
ET	Extratropical transition
FOV	Field of view
GLM	Geostationary Lightning Mapper
GMI	GPM microwave imager
GPM	Global Precipitation Measurement
GPM-CO	Global Precipitation Measurement-Core Observatory
IBTrACS	Internation Best Track Archive for Climate Stewardship
IC	Intra-cloud
ITP	Individual time period
LEO	Low Earth-orbiting
MSLP	Minimum sea level pressure
MSW	Maximum wind speed
PF	Precipitation feature
PCT	Polarization corrected temperature
PTC	Post-tropical cyclone
RMW	Radius of maximum wind
rPF	Radar-derived precipitation feature (from the GPM-CO)

Table A1
Continued

Acronym	Meaning
Tb	Brightness temperature
TC	Tropical cyclone
TRMM-LIS	Tropical Rainfall Measuring Mission-Lightning Imaging Sensor
TS	Tropical storm
TSR	Tropical storm force radius
VLF	Very low-frequency

Data Availability Statement

All GPM precipitation feature data is available at http://atmos.tamucc.edu/trmm/data/gpm/ (Liu, 2017). The GLM data are available via the National Oceanic and Atmospheric Administration (NOAA) Comprehensive Large Array-data Stewardship System (CLASS) at https://www.avl.class.noaa.gov/saa/products/welcome (NOAA, 2021). The IBTrACS Tropical Cyclone data is available via https://www.ncei.noaa.gov/products/international-best-track-archive (Knapp et al., 2018). ERA5 reanalysis data is available from the Copernicus Climate Data store at https://cds.climate.copernicus.eu/#!/home (Copernicus Climate Change Service, 2017).

Acknowledgments
This work was supported by NASA MSCF Award NNM11AA01A and the late Dr. Gail Skofronick-Jackson with continued support from Dr. Will McCarty through NASA's Internal Scientist Funding Model in the Weather and Atmospheric Dynamics Program at NASA Headquarters. We would like to thank Dr. Chuntao Liu at Texas A&M Corpus Christi for providing the GPM PF data sets and three anonymous reviewers whose suggestions substantially improved this paper.

References

Abarca, S. F., Corbosiero, K. L., & Vollaro, D. (2011). The World Wide lightning location network and convective activity in tropical cyclones. *Monthly Weather Review*, *139*(1), 175–191. https://doi.org/10.1175/2010MWR3383.1

Alvey, G. R., Zawislak, J., & Zipser, E. J. (2015). Precipitation properties observed during tropical cyclone intensity change. *Monthly Weather Review*, *143*(11), 4476–4492. https://doi.org/10.1175/MWR-D-15-0065.1

Bateman, M., & Mach, D. (2020). Preliminary detection efficiency and false alarm rate assessment of the Geostationary Lightning Mapper on the GOES-16 satellite. *Journal of Applied Remote Sensing*, *14*(03), 1–10. https://doi.org/10.1117/1.jrs.14.032406

Bian, G. F., Nie, G. Z., & Qiu, X. (2021). How well is outer tropical cyclone size represented in the ERA5 reanalysis dataset? *Atmospheric Research*, *249*, 105339. https://doi.org/10.1016/j.atmosres.2020.105339

Black, M. L., Burpee, R. W., & Marks, F. D. (1996). Vertical motion characteristics of tropical cyclones determined with airborne Doppler radial velocities. *Journal of the Atmospheric Sciences*, *53*(13), 1887–1909. https://doi.org/10.1175/1520-0469(1996)053<1887:VMCOTC>2.0.CO;2

Blake, E. S., Kimberlain, T. B., Berg, R. J., Cangialosi, J. P., & Benven, J. L. (2013). Tropical cyclone report: Hurricane Sandy.

Boccippio, D. J., Goodman, S. J., & Heckman, S. (2000). Regional differences in tropical lightning distributions. *Journal of Applied Meteorology*, *39*(12), 2231–2248. https://doi.org/10.1175/1520-0450(2001)040<2231:RDITLD>2.0.CO;2

Bruning, E. C., & MacGorman, D. R. (2013). Theory and observations of controls on lightning flash size spectra. *Journal of the Atmospheric Sciences*, *70*(12), 4012–4029. https://doi.org/10.1175/JAS-D-12-0289.1

Carey, L. D., Murphy, M. J., McCormick, T. L., & Demetriades, N. W. S. (2005). Lightning location relative to storm structure in a leading-line, trailing-stratiform mesoscale convective system. *Journal of Geophysical Research*, *110*(3), 1–23. https://doi.org/10.1029/2003JD004371

Carey, L. D., & Rutledge, S. A. (1996). A multiparameter radar case study of the microphysical and kinematic evolution of a lightning producing storm. *Meteorology and Atmospheric Physics*, *59*(1–2), 33–64. https://doi.org/10.1007/BF01032000

Carey, L. D., & Rutledge, S. A. (2000). The relationship between precipitation and lightning in tropical island convection: A C-band polarimetric radar study. *Monthly Weather Review*, *128*(8), 2687–2710. https://doi.org/10.1175/1520-0493(2000)128<2687:TRBPAL>2.0.CO;2

Carey, L. D., Schultz, E. V., Schultz, C. J., Deierling, W., Petersen, W. A., Bain, A. L., & Pickering, K. E. (2019). An evaluation of relationships between radar-inferred kinematic and microphysical parameters and lightning flash rates in Alabama storms. *Atmosphere*, *10*(12), 1–36. https://doi.org/10.3390/atmos10120796

Carlomusto, M. (2019). GOES-R series product definition and users' guide. *NASA, 416-R-PUG-GRB-0348 Vol. 4, Rev 2.2*, *5*.

Cecil, D. J., & Zipser, E. J. (1999). Relationships between tropical cyclone intensity and satellite-based indicators of inner core convection: 85-GHz ice-scattering signature and lightning. *Monthly Weather Review*, *127*(1), 103–123. https://doi.org/10.1175/1520-0493(1999)127<0103:rbtcia>2.0.co;2

Cecil, D. J., & Zipser, E. J. (2002). Reflectivity, ice scattering, and lightning characteristics of hurricane eyewalls and rainbands. Part II: Intercomparison of observations. *Monthly Weather Review*, *130*(4), 785–801. https://doi.org/10.1175/1520-0493(2002)130<0785:RISALC>2.0.CO;2

Cecil, D. J., Zipser, E. J., & Nesbitt, S. W. (2002). Reflectivity, ice scattering, and lightning characteristics of hurricane eyewalls and rainbands. Part I: Quantitative description. *Monthly Weather Review*, *130*(4), 769–784. https://doi.org/10.1175/1520-0493(2002)130<0769:RISALC>2.0.CO;2

Christian, H. J., Blakeslee, R. J., Boccippio, D. J., Boeck, W. L., Buechler, D. E., Driscoll, K. T., et al. (2003). Global frequency and distribution of lightning as observed from space by the optical transient detector. *Journal of Geophysical Research*, *108*(D1), 1–15. https://doi.org/10.1029/2002JD002347

Christian, H. J., Blakeslee, R. J., & Goodman, S. J. (1992). *Lightning imaging sensor (LIS) for the Earth observing system*. NASA, Scientific and Technical Information Program.

Copernicus Climate Change Service. (2017). ERA5: Fifth generation of ECMWF atmospheric reanalyses of the global climate. [Dataset]. https://cds.climate.copernicus.eu/#!/search?text=ERA5&type=dataset

Corbosiero, K. L., & Molinari, J. (2002). The effects of vertical wind shear on the distribution of convection in tropical cyclones. *Monthly Weather Review*, *130*(8), 2110–2123. https://doi.org/10.1175/1520-0493(2002)130<2110:TEOVWS>2.0.CO;2

Corbosiero, K. L., & Molinari, J. (2003). The relationship between storm motion, vertical wind shear, and convective asymmetries in tropical cyclones. *Journal of the Atmospheric Sciences*, *60*(2), 366–376. https://doi.org/10.1175/1520-0469(2003)060<0366:TRBSMV>2.0.CO;2

DeHart, J. C., Houze, R. A., & Rogers, R. F. (2014). Quadrant distribution of tropical cyclone inner-core kinematics in relation to environmental shear. *Journal of the Atmospheric Sciences*, *71*(7), 2713–2732. https://doi.org/10.1175/JAS-D-13-0298.1

Deierling, W., & Petersen, W. A. (2008). Total lightning activity as an indicator of updraft characteristics. *Journal of Geophysical Research*, *113*(D16), 1–11. https://doi.org/10.1029/2007JD009598

DeMaria, M., DeMaria, R. T., Knaff, J. A., & Molenar, D. (2012). Tropical cyclone lightning and rapid intensity change. *Monthly Weather Review*, *140*(6), 1828–1842. https://doi.org/10.1175/MWR-D-11-00236.1

Dullaart, J. C. M., Muis, S., Bloemendaal, N., & Aerts, J. C. J. H. (2020). Advancing global storm surge modelling using the new ERA5 climate reanalysis. *Climate Dynamics*, *54*(1–2), 1007–1021. https://doi.org/10.1007/s00382-019-05044-0

Dye, J. E., & Bansemer, A. (2019). Electrification in mesoscale updrafts of deep stratiform and anvil clouds in Florida. *Journal of Geophysical Research: Atmospheres*, *124*(2), 1021–1049. https://doi.org/10.1029/2018JD029130

Dye, J. E., Jones, J. J., Weinheimer, A. J., & Winn, W. P. (1988). Observations within two regions of charge during initial thunderstorm electrification. *Quarterly Journal of the Royal Meteorological Society*, *114*(483), 1271–1290. https://doi.org/10.1002/qj.49711448306

Evans, C., & Hart, R. E. (2008). Analysis of the wind field evolution associated with the extratropical transition of Bonnie (1998). *Monthly Weather Review*, *136*(6), 2047–2065. https://doi.org/10.1175/2007MWR2051.1

Evans, C., Wood, K. M., Aberson, S. D., Archambault, H. M., Milrad, S. M., Bosart, L. F., et al. (2017). The extratropical transition of tropical cyclones. Part I: Cyclone evolution and direct impacts. *Monthly Weather Review*, *145*(11), 4317–4344. https://doi.org/10.1175/MWR-D-17-0027.1

Evans, J. L., & Hart, R. E. (2003). Objective indicators of the life cycle evolution of extratropical transition for Atlantic tropical cyclones. *Monthly Weather Review*, *131*(5), 909–925. https://doi.org/10.1175/1520-0493(2003)131<0909:OIOTLC>2.0.CO;2

Fierro, A. O., Shao, X. M., Hamlin, T., Reisner, J. M., & Harlin, J. (2011). Evolution of eyewall convective events as indicated by intracloud and cloud-to-ground lightning activity during the rapid intensification of Hurricanes Rita and Katrina. *Monthly Weather Review*, *139*(5), 1492–1504. https://doi.org/10.1175/2010MWR3532.1

Fierro, A. O., Stevenson, S. N., & Rabin, R. M. (2018). Evolution of GLM-observed total lightning in Hurricane Maria (2017) during the period of maximum intensity. *Monthly Weather Review*, *146*(6), 1641–1666. https://doi.org/10.1175/MWR-D-18-0066.1

Foley, G. R., & Hanstrum, B. N. (1994). The capture of tropical cyclones by cold fronts off the west coast of Australia. *Weather and Forecasting*, *9*(4), 577–592. https://doi.org/10.1175/1520-0434(1994)009<0577:TCOTCB>2.0.CO;2

Frank, W. M., & Ritchie, E. A. (2001). Effects of vertical wind shear on the intensity and structure of numerically simulated hurricanes. *Monthly Weather Review*, *129*(9), 2249–2269. https://doi.org/10.1175/1520-0493(2001)129<2249:EOVWSO>2.0.CO;2

Fritz, C., Wang, Z., Nesbitt, S. W., & Dunkerton, T. J. (2016). Vertical structure and contribution of different types of precipitation during Atlantic tropical cyclone formation as revealed by TRMM PR. *Geophysical Research Letters*, *43*(2), 894–901. https://doi.org/10.1002/2015GL067122

Goodman, S. J., Blakeslee, R. J., Koshak, W. J., Mach, D., Bailey, J., Buechler, D. E., et al. (2013). The GOES-R geostationary lightning mapper (GLM). *Atmospheric Research*, *125–126*, 34–49. https://doi.org/10.1016/j.atmosres.2013.01.006

Goodman, S. J., Buechler, D. E., Wright, P. D., & David, W. (1988). Lightning and precipitation history of a microburst-producing storm. *Geophysical Research Letters*, *15*(11), 1185–1188. https://doi.org/10.1029/GL015i011p01185

Gramcianinov, C. B., Campos, R. M., de Camargo, R., Hodges, K. I., Guedes Soares, C., & da Silva Dias, P. L. (2020). Analysis of Atlantic extratropical storm tracks characteristics in 41 years of ERA5 and CFSR/CFSv2 databases. *Ocean Engineering*, *216*(July), 108111. https://doi.org/10.1016/j.oceaneng.2020.108111

Griffin, E. M., Schuur, T. J., MacGorman, D. R., Kumjian, M. R., & Fierro, A. O. (2014). An electrical and polarimetric analysis of the overland reintensification of Tropical Storm Erin (2007). *Monthly Weather Review*, *142*(6), 2321–2344. https://doi.org/10.1175/MWR-D-13-00360.1

Hart, R. E. (2003). A cyclone phase space derived from thermal wind and thermal asymmetry. *Monthly Weather Review*, *131*(4), 585–616. https://doi.org/10.1175/1520-0493(2003)131<0585:ACPSDF>2.0.CO;2

Hart, R. E., & Evans, J. L. (2001). A climatology of the extratropical transition of Atlantic tropical cyclones. *Journal of Climate*, *14*(4), 546–564. https://doi.org/10.1175/1520-0442(2001)014<0546:ACOTET>2.0.CO;2

Hazelton, A. T., & Hart, R. E. (2013). Hurricane eyewall slope as determined from airborne radar reflectivity data: Composites and case studies. *Weather and Forecasting*, *28*(2), 368–386. https://doi.org/10.1175/WAF-D-12-00037.1

Hence, D. A., & Houze, R. A. (2011). Vertical structure of hurricane eyewalls as seen by the TRMM Precipitation Radar. *Journal of the Atmospheric Sciences*, *68*(8), 1637–1652. https://doi.org/10.1175/2011JAS3578.1

Hence, D. A., & Houze, R. A. (2012). Vertical structure of tropical cyclones with concentric eyewalls as seen by the TRMM precipitation radar. *Journal of the Atmospheric Sciences*, *69*(3), 1021–1036. https://doi.org/10.1175/JAS-D-11-0119.1

Hersbach, H., Bell, B., Berrisford, P., Hirahara, S., Horányi, A., Muñoz-Sabater, J., et al. (2020). The ERA5 global reanalysis. *Quarterly Journal of the Royal Meteorological Society*, *146*(730), 1999–2049. https://doi.org/10.1002/qj.3803

Heuscher, L., Liu, C., Gatlin, P. N., & Petersen, W. A. (2022). Relationship between lightning, precipitation, and environmental characteristics at mid-/high latitudes from a GLM and GPM perspective. *Journal of Geophysical Research: Atmospheres*, *127*(13), 1–17. https://doi.org/10.1029/2022JD036894

Hodges, K. I., & Emerton, R. (2015). The prediction of Northern Hemisphere tropical cyclone extended life cycles by the ECMWF ensemble and deterministic prediction systems. Part I: Tropical cyclone stage. *Monthly Weather Review*, *143*(12), 5091–5114. https://doi.org/10.1175/MWR-D-13-00385.1

Hou, A. Y., Kakar, R. K., Neeck, S., Azarbarzin, A. A., Kummerow, C. D., Kojima, M., et al. (2014). The global precipitation measurement mission. *Bulletin of the American Meteorological Society*, *95*(May), 701–722. https://doi.org/10.1175/BAMS-D-13-00164.1

Houze, R. A. (2010). Clouds in tropical cyclones. *Monthly Weather Review*, *138*(2), 293–344. https://doi.org/10.1175/2009MWR2989.1

Houze, R. A., Wilton, D. C., & Smull, B. F. (2007). Monsoon convection in the Himalayan region as seen by the TRMM precipitation radar. *Quarterly Journal of the Royal Meteorological Society*, *133*(627), 1389–1411. https://doi.org/10.1002/qj.106

Hu, J., Rosenfeld, D., Ryzhkov, A. V., & Zhang, P. (2020). Synergetic use of the WSR-88D radars, GOES-R satellites, and lightning networks to study microphysical characteristics of hurricanes. *Journal of Applied Meteorology and Climatology*, *59*(6), 1051–1068. https://doi.org/10.1175/JAMC-D-19-0122.1

Iguchi, T., Hanado, H., Takahashi, N., Kobayashi, S., & Satoh, S. (2003). The Dual-frequency precipitation radar for the GPM core satellite. In *International Geoscience and Remote Sensing Symposium (IGARSS)* (Vol. 3, pp. 1698–1700). https://doi.org/10.1109/igarss.2003.1294221

Jiang, H., Liu, C., & Zipser, E. J. (2011). A TRMM-based tropical cyclone cloud and precipitation feature database. *Journal of Applied Meteorology and Climatology*, *50*(6), 1255–1274. https://doi.org/10.1175/2011JAMC2662.1

Jiang, H., & Ramirez, E. M. (2013). Necessary conditions for tropical cyclone rapid intensification as derived from 11 years of TRMM data. *Journal of Climate*, *26*(17), 6459–6470. https://doi.org/10.1175/JCLI-D-12-00432.1

Jiang, H., Ramirez, E. M., & Cecil, D. J. (2013). Convective and rainfall properties of tropical cyclone inner cores and rainbands from 11 years of TRMM data. *Monthly Weather Review*, *141*(2), 431–450. https://doi.org/10.1175/MWR-D-11-00360.1

Jiang, H., Zagrodnik, J. P., Tao, C., & Zipser, E. J. (2018). Classifying precipitation types in tropical cyclones using the NRL 37 GHz color product. *Journal of Geophysical Research: Atmospheres*, *123*(10), 5509–5524. https://doi.org/10.1029/2018JD028324

Jorgensen, D. P. (1984). Mesoscale and convective-scale characteristics of mature hurricanes. Part I: General observations by research aircraft. *Journal of the Atmospheric Sciences*, *41*(8), 1268–1285. https://doi.org/10.1175/1520-0469(1984)041<1268:MACSCO>2.0.CO;2

Jorgensen, D. P., Zipser, E. J., & LeMone, M. A. (1985). Vertical motions in intense hurricanes. *Journal of the Atmospheric Sciences*, *42*(8), 839–856. https://doi.org/10.1175/1520-0469(1985)042<0839:VMIIH>2.0.CO;2

Kasahara, M., Imaoka, K., Kachi, M., Fujii, H., Naoki, K., Maeda, T., et al. (2012). Status of AMSR2 on GCOM-W1. In *Sensors, systems, and next-generation satellites XVI* (Vol. 8533). https://doi.org/10.1117/12.975810

Kimball, S. K., & Mulekar, M. S. (2004). A 15-year climatology of North Atlantic tropical cyclones. Part I: Size parameters. *Journal of Climate*, *17*(18), 3555–3575. https://doi.org/10.1175/1520-0442(2004)017<3555:AYCONA>2.0.CO;2

Klein, P. M. (1997). *Extratropical transition of western North Pacific tropical cyclones*. Naval Postgraduate School.

Klein, P. M., Harr, P. A., & Elsberry, R. L. (2000). Extratropical transition of western North Pacific tropical cyclones: An overview and conceptual model of the transformation stage. *Weather and Forecasting*, *15*(4), 373–395. https://doi.org/10.1175/1520-0434(2000)015<0373:ETOWNP>2.0.CO;2

Knaff, J. A., Sampson, C. R., DeMaria, M., Marchok, T. P., Gross, J. M., & McAdie, C. J. (2007). Statistical tropical cyclone wind radii prediction using climatology and persistence. *Weather and Forecasting*, *22*(4), 781–791. https://doi.org/10.1175/WAF1026.1

Knapp, K. R. (2019). *International best track archive for climate stewardship (IBTrACS)*. Technical documentation. National Oceanic and Atmospheric Administration, National Climatic Data Center.

Knapp, K. R., Diamond, H. J., Kossin, J. P., Kruk, M. C., & Schreck, C. J. (2018). International best track archive for climate stewardship (IBTrACS) project, version 4. [Dataset]. NOAA National Centers for Environmental Information. https://doi.org/10.25921/82ty-9e16

Knapp, K. R., & Kruk, M. C. (2010). Quantifying interagency differences in tropical cyclone best-track wind speed estimates. *Monthly Weather Review*, *138*(4), 1459–1473. https://doi.org/10.1175/2009MWR3123.1

Kummerow, C. D. (1998). Beamfilling errors in passive microwave rainfall retrievals. *Journal of Applied Meteorology and Climatology*, *37*(4), 356–370. https://doi.org/10.1175/1520-0450(1998)037<0356:BEIPMR>2.0.CO;2

Landsea, C. W., & Franklin, J. L. (2013). Atlantic hurricane database uncertainty and presentation of a new database format. *Monthly Weather Review*, *141*(10), 3576–3592. https://doi.org/10.1175/MWR-D-12-00254.1

Lang, T. J., Rutledge, S. A., & Wiens, K. C. (2004). Origins of positive cloud-to-ground lightning flashes in the stratiform region of a mesoscale convective system. *Geophysical Research Letters*, *31*(10), 1–4. https://doi.org/10.1029/2004GL019823

Lee, T. F., Turk, F. J., Hawkins, J., & Richardson, K. (2002). Interpretation of TRMM TMI images of tropical cyclones. *Earth Interactions*, *6*(3), 1–17. https://doi.org/10.1175/1087-3562(2002)006<0001:iottio>2.0.co;2

Liu, C. (2017). GPM precipitation feature dataset. [Dataset]. http://atmos.tamucc.edu/trmm/data/gpm/

Liu, C., Cecil, D. J., & Zipser, E. J. (2011). Relationships between lightning flash rates and passive microwave brightness temperatures at 85 and 37 GHz over the tropics and subtropics. *Journal of Geophysical Research*, *116*(D23), 1–14. https://doi.org/10.1029/2011JD016463

Liu, C., Zipser, E. J., Cecil, D. J., Nesbitt, S. W., & Sherwood, S. (2008). A cloud and precipitation feature database from nine years of TRMM observations. *Journal of Applied Meteorology and Climatology*, *47*(10), 2712–2728. https://doi.org/10.1175/2008JAMC1890.1

Logan, T. (2021). An analysis of the performance of the Houston lightning mapping array during an intense period of convection during tropical storm Harvey. *Journal of Geophysical Research: Atmospheres*, *126*(3), 1–18. https://doi.org/10.1029/2020JD033270

Lord, S. J., Willoughby, H. E., & Piotrowicz, J. M. (1984). Role of a parameterized ice-phase microphysics in an axisymmetric, nonhydrostatic tropical cyclone model. *Journal of the Atmospheric Sciences*, *41*(19), 2836–2848. https://doi.org/10.1175/1520-0469(1984)041<2836:ROAPIP>2.0.CO;2

Lyons, W. A., & Keen, C. S. (1994). Observations of lightning in convective supercells within tropical storms and hurricanes. *Monthly Weather Review*, *122*(8), 1897–1916. https://doi.org/10.1175/1520-0493(1994)122<1897:OOLICS>2.0.CO;2

Malakar, P., Kesarkar, A. P., Bhate, J. N., Singh, V., & Deshamukhya, A. (2020). Comparison of reanalysis data sets to comprehend the evolution of tropical cyclones over North Indian Ocean. *Earth and Space Science*, *7*(2), 1–15. https://doi.org/10.1029/2019EA000978

Marchand, M., Hilburn, K. A., & Miller, S. D. (2019). Geostationary lightning mapper and Earth networks lightning detection over the contiguous United States and dependence on flash characteristics. *Journal of Geophysical Research: Atmospheres*, *124*(21), 11552–11567. https://doi.org/10.1029/2019JD031039

Marks, F. D., & Houze, R. A. (1987). Inner core structure of Hurricane Alicia from airborne Doppler radar observations. *Journal of the Atmospheric Sciences*, *44*(9), 1296–1317. https://doi.org/10.1175/1520-0469(1987)044<1296:ICSOHA>2.0.CO;2

Matyas, C. (2010). Locating convection in landfalling tropical cyclones: A GIS-based analysis of radar reflectivities and comparison to lightning-based observations. *Physical Geography*, *31*(5), 385–406. https://doi.org/10.2747/0272-3646.31.5.385

May, P. T., Kepert, J. D., & Keenan, T. D. (2008). Polarimetric radar observations of the persistently asymmetric structure of Tropical Cyclone Ingrid. *Monthly Weather Review*, *136*(2), 616–630. https://doi.org/10.1175/2007MWR2077.1

Meltzer, R., Ellen, I. G., & Li, X. (2021). Localized commercial effects from natural disasters: The case of Hurricane Sandy and New York City. *Regional Science and Urban Economics*, *86*(April 2020), 103608. https://doi.org/10.1016/j.regsciurbeco.2020.103608

Molinari, J., Moore, P. K., & Idone, V. P. (1999). Convective structure of hurricanes as revealed by lightning locations. *Monthly Weather Review*, *127*(4), 520–534. https://doi.org/10.1175/1520-0493(1999)127<0520:CSOHAR>2.0.CO;2

Molinari, J., Moore, P. K., Idone, V. P., Henderson, R. W., & Saljoughy, A. B. (1994). Cloud-to-ground lightning in hurricane Andrew. *Journal of Geophysical Research*, *99*(D8), 16665–16676. https://doi.org/10.1029/94JD00722

Morin, M. J., & Parker, M. D. (2011). A numerical investigation of supercells in landfalling tropical cyclones. *Geophysical Research Letters*, *38*(10), 1–7. https://doi.org/10.1029/2011GL047448

NASA. (2023). AMSR-E | aqua project science. Retrieved from https://aqua.nasa.gov/amsr-e

Nesbitt, S. W., Zipser, E. J., & Cecil, D. J. (2000). A census of precipitation features in the tropics using TRMM: Radar, ice scattering, and lightning observations. *Journal of Climate*, *13*(23), 4087–4106. https://doi.org/10.1175/1520-0442(2000)013<4087:ACOPFI>2.0.CO;2

NOAA. (2021). NOAA's comprehensive large array-data stewardship system. [Dataset]. https://www.avl.class.noaa.gov/saa/products/search?sub_id=0&datatype_family=GRGLMPROD&submit.x=28&submit.y=5

Oki, T., Imaoka, K., & Kachi, M. (2010). AMSR instruments on GCOM-W1/2: Concepts and applications. In *2010 IEEE international geoscience and remote sensing symposium* (pp. 1363–1366). IEEE. https://doi.org/10.1109/IGARSS.2010.5650001

Pan, L., Qie, X., Liu, D., Wang, D., & Yang, J. (2010). The lightning activities in super typhoons over the Northwest Pacific. *Science China Earth Sciences*, *53*(8), 1241–1248. https://doi.org/10.1007/s11430-010-3034-z

Petersen, W. A., Rutledge, S. A., & Orville, R. E. (1996). Cloud-to-ground lightning observations from TOGA COARE: Selected results and lightning location algorithms. *Monthly Weather Review*, *124*(4), 602–620. https://doi.org/10.1175/1520-0493(1996)124<0602:CTGLOF>2.0.CO;2

Ringhausen, J. S., & Bitzer, P. M. (2021). An in-depth analysis of lightning trends in Hurricane Harvey using satellite and ground-based measurements. *Journal of Geophysical Research: Atmospheres*, *126*(7), 1–26. https://doi.org/10.1029/2020jd032859

Rogers, R. F., Lorsolo, S., Reasor, P. D., Gamache, J. F., & Marks, F. D. (2012). Multiscale analysis of tropical cyclone kinematic structure from airborne Doppler radar composites. *Monthly Weather Review*, *140*(1), 77–99. https://doi.org/10.1175/MWR-D-10-05075.1

Rogers, R. F., Zhang, J. A., Zawislak, J., Jiang, H., Alvey, G. R., Zipser, E. J., & Stevenson, S. N. (2016). Observations of the structure and evolution of Hurricane Edouard (2014) during intensity change. Part II: Kinematic structure and the distribution of deep convection. *Monthly Weather Review*, *144*(9), 3355–3376. https://doi.org/10.1175/MWR-D-16-0017.1

Roy, A., Noy, I., & Cuffe, H. E. (2022). Income and extratropical cyclones in New Zealand. *Journal of Environmental Management*, *311*, 114852. https://doi.org/10.1016/j.jenvman.2022.114852

Rudlosky, S. D., Goodman, S. J., Virts, K. S., & Bruning, E. C. (2019). Initial geostationary lightning mapper observations. *Geophysical Research Letters*, *46*(2), 1097–1104. https://doi.org/10.1029/2018GL081052

Rudlosky, S. D., & Virts, K. S. (2021). Dual geostationary lightning mapper observations. *Monthly Weather Review*, *149*(4), 979–998. https://doi.org/10.1175/mwr-d-20-0242.1

Rutledge, S. A., Hilburn, K. A., Clayton, A., Fuchs, B. R., & Miller, S. D. (2020). Evaluating Geostationary Lightning Mapper flash rates within intense convective storms. *Journal of Geophysical Research: Atmospheres*, *125*(14), 1–16. https://doi.org/10.1029/2020JD032827

Rutledge, S. A., & Petersen, W. A. (1994). Vertical radar reflectivity structure and cloud-to-ground lightning in the stratiform region of MCSs: Further evidence for in situ charging in the stratiform region. *Monthly Weather Review*, *122*(8), 1760–1776. https://doi.org/10.1175/1520-0493(1994)122<1760:VRRSAC>2.0.CO;2

Sainsbury, E. M., Schiemann, R. K. H., Hodges, K. I., Shaffrey, L. C., Baker, A. J., & Bhatia, K. T. (2020). How important are post-tropical cyclones for European windstorm risk? *Geophysical Research Letters*, *47*(18), 1–9. https://doi.org/10.1029/2020GL089853

Samsury, C. E., & Orville, R. E. (1994). Cloud-to-ground lightning in tropical cyclones: A study of hurricanes Hugo (1989) and Jerry (1989). *Monthly Weather Review*, *122*(8), 1887–1896. https://doi.org/10.1175/1520-0493(1994)122<1887:CTGLIT>2.0.CO;2

Sarro, G., & Evans, C. (2022). An updated investigation of post-transformation intensity, structural, and duration extremes for extratropically transitioning North Atlantic tropical cyclones. *Monthly Weather Review*, *150*(11), 2911–2933. https://doi.org/10.1175/mwr-d-22-0088.1

Schenkel, B. A., Calhoun, K. M., Sandmæl, T. N., Fruits, Z. R., Schick, I., Ake, M. C., & Kassel, B. F. (2023). Lightning and radar characteristics of tornadic cells in landfalling tropical cyclones. *Journal of Geophysical Research: Atmospheres*, *128*(16), e2023JD038685. https://doi.org/10.1029/2023JD038685

Schultz, C. J., Petersen, W. A., & Carey, L. D. (2011). Lightning and severe weather: A comparison between total and cloud-to-ground lightning trends. *Weather and Forecasting*, *26*(5), 744–755. https://doi.org/10.1175/WAF-D-10-05026.1

Schuur, T. J., & Rutledge, S. A. (2000). Electrification of stratiform regions in Mesoscale Convective Systems. Part II: Two-dimensional numerical model simulations of a symmetric MCS. *Journal of the Atmospheric Sciences*, *57*(13), 1983–2006. https://doi.org/10.1175/1520-0469(2000)057<1961:EOSRIM>2.0.CO;2

Serra, Y. L., Kiladis, G. N., & Hodges, K. I. (2010). Tracking and mean structure of easterly waves over the Intra-Americas Sea. *Journal of Climate*, *23*(18), 4823–4840. https://doi.org/10.1175/2010JCLI3223.1

Shao, X. M., Harlin, J., Stock, M., Stanley, M., Regan, A., Wiens, K. C., et al. (2005). Katrina and Rita were lit up with lightning. *Eos*, *86*(42), 398. https://doi.org/10.1029/2005EO420004

Shao, X. M., Stanley, M., Regan, A., Harlin, J., Pongratz, M., & Stock, M. (2006). Total lightning observations with the new and improved Los Alamos Sferic array (LASA). *Journal of Atmospheric and Oceanic Technology*, *23*(10), 1273–1288. https://doi.org/10.1175/JTECH1908.1

Shea, D. J., & Gray, W. M. (1973). The hurricane's inner core region. I. Symmetric and asymmetric structure. *Journal of the Atmospheric Sciences*, *30*(8), 1544–1564. https://doi.org/10.1175/1520-0469(1973)030<1544:THICRI>2.0.CO;2

Slocum, C. J., Knaff, J. A., & Stevenson, S. N. (2023). Lightning-based tropical cyclone rapid intensification guidance. *Weather and Forecasting*, *38*(7), 1209–1227. https://doi.org/10.1175/WAF-D-22-0164.1

Squires, K., & Businger, S. (2008). The morphology of eyewall lightning outbreaks in two Category 5 hurricanes. *Monthly Weather Review*, *136*, 1706–1726. https://doi.org/10.1175/2007MWR2150.1

Stern, D. P., & Nolan, D. S. (2009). Reexamining the vertical structure of tangential winds in tropical cyclones: Observations and theory. *Journal of the Atmospheric Sciences*, *66*(12), 3579–3600. https://doi.org/10.1175/2009JAS2916.1

Stevenson, S. N., Corbosiero, K. L., & Abarca, S. F. (2016). Lightning in eastern North Pacific tropical cyclones: A comparison to the north Atlantic. *Monthly Weather Review*, *144*(1), 225–239. https://doi.org/10.1175/MWR-D-15-0276.1

Stevenson, S. N., Corbosiero, K. L., DeMaria, M., & Vigh, J. L. (2018). A 10-year survey of tropical cyclone inner-core lightning bursts and their relationship to intensity change. *Weather and Forecasting*, *33*(1), 23–36. https://doi.org/10.1175/WAF-D-17-0096.1

Stevenson, S. N., Corbosiero, K. L., & Molinari, J. (2014). The convective evolution and rapid intensification of Hurricane Earl (2010). *Monthly Weather Review*, *142*(11), 4364–4380. https://doi.org/10.1175/MWR-D-14-00078.1

Stewart, S. R. (2018). Tropical cyclone report: Hurricane Ophelia.

Stolzenburg, M., Marshall, T. C., Rust, W. D., & Smull, B. F. (1994). Horizontal distribution of electrical and meteorological conditions across the stratiform region of a mesoscale convective system. *Monthly Weather Review*, *122*(8), 1777–1797. https://doi.org/10.1175/1520-0493(1994)122<1777:HDOEAM>2.0.CO;2

Tao, C., & Jiang, H. (2015). Distributions of shallow to very deep precipitation-convection in rapidly intensifying tropical cyclones. *Journal of Climate*, *28*(22), 8791–8824. https://doi.org/10.1175/JCLI-D-14-00448.1

Tao, C., Jiang, H., & Zawislak, J. (2017). The relative importance of stratiform and convective rainfall in rapidly intensifying tropical cyclones. *Monthly Weather Review*, *145*(3), 795–809. https://doi.org/10.1175/MWR-D-16-0316.1

Torn, R. D., & Snyder, C. (2012). Uncertainty of tropical cyclone best-track information. *Weather and Forecasting*, *27*(3), 715–729. https://doi.org/10.1175/WAF-D-11-00085.1

Wang, F., Qie, X., Liu, D., Shi, H., & Srivastava, A. (2016). Lightning activity and its relationship with typhoon intensity and vertical wind shear for Super Typhoon Haiyan (1330). *ResearchGate*, *30*(1), 117–127. https://doi.org/10.1007/s13351-016-4228-x

Wang, F., Qie, X., Wang, D., & Srivastava, A. (2018). Lightning activity in tropical cyclones and its relationship to dynamic and thermodynamic parameters over the northwest Pacific. *Atmospheric Research*, *213*(February), 86–96. https://doi.org/10.1016/j.atmosres.2018.05.027

Williams, E. R., Rothkin, K., Stevenson, D., & Boccippio, D. J. (2000). Global lightning variations caused by changes in thunderstorm flash rate and by changes in the number of thunderstorms. *Journal of Applied Meteorology*, *39*(12), 2223–2230. https://doi.org/10.1175/1520-0450(2001)040<2223:glvcbc>2.0.co;2

Williams, E. R., & Stanfill, S. (2002). The physical origin of the land – Ocean contrast in lightning activity. *C. R. Physique*, *3*(10), 1277–1292. https://doi.org/10.1016/S1631-0705(02)01407-X

Xu, W., Rutledge, S. A., & Zhang, W. (2017). Relationships between total lightning, deep convection, and tropical cyclone intensity change. *Journal of Geophysical Research: Atmospheres*, *122*(13), 7047–7063. https://doi.org/10.1002/2017JD027072

Yang, S., Bankert, R., & Cossuth, J. (2020). Tropical cyclone climatology from satellite passive microwave measurements. *Remote Sensing*, *12*(21), 1–20. https://doi.org/10.3390/rs12213610

Yuter, S. E., & Houze, R. A. (1995). Three-dimensional kinematic and microphysical evolution of Florida cumulonimbus. Part I: Spatial distribution of updrafts, downdrafts, and precipitation. *Monthly Weather Review*, *123*(7), 1921–1940. https://doi.org/10.1175/1520-0493

Zhang, D., & Cummins, K. L. (2020). Time evolution of satellite-based optical properties in lightning flashes, and its impact on GLM flash detection. *Journal of Geophysical Research: Atmospheres*, *125*(6), 1–17. https://doi.org/10.1029/2019JD032024

Zhang, W., Zhang, Y., Zheng, D., Wang, F., & Xu, L. (2015). Relationship between lightning and tropical cyclone intensity over the northwest Pacific. *Journal of Geophysical Research: Atmospheres*, *120*(9), 4072–4089. https://doi.org/10.1002/2014JD022334

Zhong, R., Yang, Q., Hodges, K. I., Wu, R., & Chen, D. (2023). Impact of data resolution on tracking Southern Ocean cyclones. *Monthly Weather Review*, *151*(1), 3–22. https://doi.org/10.1175/mwr-d-22-0121.1

Zipser, E. J., & Lutz, K. R. (1994). The vertical profile of radar reflectivity of convective cells: A strong indicator of storm intensity and lightning probability? *Monthly Weather Review*, *122*(8), 1751–1759. https://doi.org/10.1175/1520-0493(1994)122<1751:TVPORR>2.0.CO;2